

## **MRI Field-transfer Reconstruction with Limited Data: Regularization by Neural Style Transfer**

Guoyao Shen <sup>[1, 2]</sup>, Yancheng Zhu <sup>[1]</sup>, Hernan Jara <sup>[3]</sup>, Sean B. Andersson <sup>[1, 4]</sup>, Chad W. Farris <sup>[3]</sup>,  
Stephan Anderson <sup>[2, 3]</sup>, Xin Zhang\*<sup>[1, 2]</sup>

[1] Department of Mechanical Engineering, Boston University, Boston, MA 02215.

[2] The Photonics Center, Boston University, Boston, MA 02215.

[3] Department of Radiology, Boston Medical Center and Boston University Chobanian & Avedisian School of Medicine, Boston, MA, 02118.

[4] Department of Systems Engineering, Boston University, Boston, MA 02215.

\*Corresponding author: Prof. Xin Zhang, email: [xinz@bu.edu](mailto:xinz@bu.edu)

**Acknowledgments:** This work was supported by the Rajen Kilachand Fund for Integrated Life Science and Engineering. We would like to thank the Boston University Photonics Center for technical support.

Our code is available at: [https://github.com/GuoyaoShen/RNST-Regularization\\_by\\_NST](https://github.com/GuoyaoShen/RNST-Regularization_by_NST)

## **Abstract**

Recent works have demonstrated success in MRI reconstruction using deep learning-based models. However, most reported approaches require training on a task-specific, large-scale dataset. Regularization by denoising (RED) is a general pipeline which embeds a denoiser as a prior for image reconstruction. The potential of RED has been demonstrated for multiple image-related tasks such as denoising, deblurring and super-resolution. In this work, we propose a regularization by neural style transfer (RNST) method to further leverage the priors from the neural transfer and denoising engine. This enables RNST to reconstruct a high-quality image from a noisy low-quality image with different image styles and limited data. We validate RNST with clinical MRI scans from 1.5T and 3T and show that RNST can significantly boost image quality. Our results highlight the capability of the RNST framework for MRI reconstruction and the potential for reconstruction tasks with limited data.

## Introduction

Magnetic resonance imaging (MRI) is a critical diagnostic tool that provides invaluable diagnostic information in medicine that profoundly influences medical decision making and helps to improve patient outcomes. However, long acquisition times for MRI result in multiple limitations of this invaluable technique including motion degradation of imaging, delays in diagnosis, limited availability for patient access, and limited ability to scan some of the sickest patients that may greatly benefit from the imaging, among others. Compressed sensing (CS) addressed this problem by acquiring less measurements in k-space. However, down-sampling in k-space usually leads to loss in image detail and misalignments. In recent years, efforts have focused on utilizing deep learning with paired datasets to train a network for deblurring reconstruction [1, 2, 3, 4, 5, 6]. However, in cases in which the original scans were performed with a lower magnetic strength or hardware with a higher magnetic strength is not available, reconstruction of a high-field-like image from the original scan may be a desirable alternative approach.

Transferring the image style from one to another while also preserving content similarities to the original style is commonly known as image domain transfer. Recently, deep learning pipelines utilizing Neural Style Transfer (NST) [7] and Generative Adversarial Network (GAN) [8] for this have been reported [9, 10, 11, 12, 13, 14, 15, 16]. Most recently, the denoising diffusion probabilistic model (DDPM) [17, 18] has also shown promising results with its sharper details. Although showing promising results in image details, GAN is also known for unstable training, while DDPM typically requires a multi-step denoising during the diffusion process. Neural style transfer includes a content loss which captures the semantic information difference and a style loss that captures the statistical correlation (Gram matrix) between the extracted feature maps in multiple layers. It seeks to minimize the combination of content and style loss and to keep a balance among the feature maps from multiple layers. A trained convolutional neural network (CNN) such as VGG19 works as a feature extraction net. Thus, the training process of the feature extraction network can be separated from the image style transfer process. This is beneficial especially when data is limited for a one-to-one pairing and provides a scalable pipeline as the style image can be changed as needed if the features are extracted properly.

Regularization by denoising (RED) is a framework that performs image reconstruction with an image denoiser as a prior [19]. As a step-forward from the Plug-and-Play Prior ( $P^3$ ) [20], RED does not rely on the ADMM optimization for chained denoising interpretation. It provides the flexibility of choosing the denoising engine and an iterative optimization procedure. As a result, RED can incorporate multiple image denoising algorithms for general image reconstruction problems. This is well-suited for our field transformation MRI reconstruction, as images from a lower magnetic strength contain more background noise with lower signal-to-noise ratio (SNR), together with a different image style when compared to a higher strength due to the difference in relaxation times. RED has shown excellent performance in multiple imaging problems with advanced denoisers. These days, the combination of the RED pipeline with deep neural networks further broadens the reconstruction task setups [21, 22, 23, 24, 25, 26].

In this work, we present an MRI magnetic field transfer reconstruction framework called regularization by neural style transfer (RNST). RNST further extends the reconstruction ability of RED by embedding a denoiser and a neural style transfer engine. As the NST engine uses a trained CNN-based feature extraction network, it does not require a large-scale paired dataset in both domains and can be pretrained separately even with differing image content than its specific task. In addition, we demonstrate that the style guidance image in NST does not have to be a paired slice, meaning that a single slice from one magnetic field can be used for the reconstruction of multiple scans in the second field. We validated our framework with 1.5T and 3T brain scans. Our results show that RNST yields promising MRI reconstructions with limited data and even more challenging background noise corruption.

## Methods

### 1. Neural style transfer

Neural style transfer (NST) is a paradigm of deep learning-based style and content separation and recombination. Consider a content image  $x_c$  and a style image  $x_s$ , NST seeks to give an output image  $x_{comb}$  which is the combination of the content and style images [7]. A deep convolutional neural network typically consists of layers of computational units which process visual information hierarchically. The output from a certain layer includes a branch of features maps. This hierarchically organized network provides a computational representation of the input image where lower layers capture pixel value details and textures while higher layers capture general image contents and shapes [7, 27, 28, 29].

NST utilizes a trained CNN network  $U_{CNN}$  to separate the style and content of the original images and recombine them in the output image so that  $x_{comb}$  is close to the  $x_c$  content-wise, while close to  $x_s$  style-wise. More specifically, consider the feature maps of an image  $x$  in layer  $l$  where they consist of  $N_l$  maps in total and each map has the size  $M_l$ . In this case, all feature maps can be represented by a matrix  $F^l \in \mathcal{R}^{N_l \times M_l}$  where  $F_{ij}^l$  corresponds to the  $i$  th feature map at position  $j$ . The content loss between the content image  $x_c$  and input image  $x$  in layer  $l$  is defined as the squared-error loss between their feature representations:

$$\mathcal{L}_{content}(x, x_c, l) = \frac{1}{2} \sum_{i,j} (F_{ij}^l - F_{c_{ij}}^l)^2 \quad (1)$$

Style loss represents the correlations between different feature maps. The correlation is given by the Gram matrix  $G^l \in \mathcal{R}^{N_l \times N_l}$ , where  $G_{ij}^l$  is the inner product of two feature maps  $i$  and  $j$  in layer  $l$ :

$$G_{ij}^l = \sum_k F_{ik}^l F_{jk}^l \quad (2)$$

Thus, the matching of the style for a given image in a certain layer is done by minimizing the mean-squared loss between the entries of Gram matrices from the style image and input image:

$$\mathcal{L}_{style}(x, x_s, l) = \frac{1}{4N_l^2 M_l^2} \sum_{i,j} (G_{ij}^l - G_{s_{ij}}^l)^2 \quad (3)$$

Then, the style loss among multiple layers is:

$$\mathcal{L}_{style}(x, x_s) = \sum_l \omega_l \mathcal{L}_{style}(x, x_s, l) \quad (4)$$

where  $\omega_l$  is the weighting factor representing the contribution of each layer. The total loss is the combination of content loss and style loss:

$$\mathcal{L}_{total}(x, x_c, x_s) = \alpha \mathcal{L}_{content}(x, x_c) + \beta \mathcal{L}_{style}(x, x_s) \quad (5)$$

where  $\alpha$  and  $\beta$  are the weighting factors of content and style loss, respectively.

## **2. Regularization by denoising (RED)**

Regularization by denoising (RED) provides a flexible pipeline for image reconstruction. Consider a classic reconstruction case where:

$$\mathbf{y} = \mathbf{H}\mathbf{x} + \mathbf{e} \quad (6)$$

here  $\mathbf{H}$  is a degradation operator and  $\mathbf{e}$  is the additional noise.  $\mathbf{x}$  represents the unknown reconstruction target and  $\mathbf{y}$  is the noisy measurement. A typical reconstruction brings the following form:

$$\hat{\mathbf{x}} = \operatorname{argmin}_x \ell(\mathbf{y}, \mathbf{x}) + \lambda \rho(\mathbf{x}) \quad (7)$$

where  $\hat{\mathbf{x}}$  is the estimated reconstruction of  $\mathbf{x}$ , and  $\ell$  and  $\rho$  are penalty and regularization terms. This form includes a branch of image reconstruction tasks such as denoising, deblurring, super-resolution, tomographic reconstruction, and so on. The noise contamination of the measurements can also be probability distributions such as Gaussian, Laplacian, or Poisson depending on the setting [19].

Previous work such as the plug-and-play prior (PnP) algorithm gives the reconstruction in a block-coordinate-descent fashion where one step is for solving the inverse problem and the other step is for denoising the updated reconstruction. While PnP does not specifically refer to a certain choice of the denoising engine as a prior, it comes with the limitation of activating a denoising algorithm and departing from the original setting without an underlying cost function [19]. As the name suggests, regularization by denoising advocates the regularization term as:

$$\rho(\mathbf{x}) = \frac{1}{2} \mathbf{x}^T (\mathbf{x} - f(\mathbf{x})) \quad (8)$$

where  $f$  refers to the denoising engine. In this way, RED comes with much more flexibility for the choice of the optimization method and denoising engine. Recent works have shown successful applications of RED for multiple reconstruction tasks accompanied by deep learning-based engines [26].

### **3.Regularization by neural style transfer (RNST)**

In this section, we propose a regularization by neural style transfer (RNST) method for magnetic field transfer reconstruction. RNST includes a neural style transfer and a denoising engine. The reconstruction from a lower-field image to a higher-field requires a process of denoising without loss of features in the tissues. However, since the original image was obtained with a lower magnetic strength, the image quality and noise level are much worse compared to the higher-field one. Though the denoising of background noise can be achieved by a denoising engine, the shifting in contrast ratio and feature loss in the reconstruction still exists. Thus, we employ an NST engine as part of our regularization optimizer to update the lower-field images iteratively such that the correlations between different features become as close as possible to the higher-field references.

Consider a magnetic field transfer reconstruction with the form of (6):

$$\mathbf{x} = \mathbf{H}\mathbf{x}_h + \mathbf{e} \quad (9)$$

where  $\mathbf{x}_h$  is the unforeseen higher-field target and  $\mathbf{x}$  is the lower-field noisy measurement. As shown in equation (7) and (8), this reconstruction process can be written in the form:

$$\hat{\mathbf{x}} = \operatorname{argmin}_x \ell(\mathbf{x}_h, \mathbf{x}) + \tau \mathbf{x}^T (\mathbf{x} - D(\mathbf{x})) \quad (10)$$

where the latter term is a regularization term with a denoiser  $D$  integrated and  $\tau$  is the corresponding weighting factor. Notice that although the degradation operator  $\mathbf{H}$  can be hard to define since modeling the imaging process from different magnetic strengths and setups is difficult, the higher-field target  $\mathbf{x}_h$  can be implicitly represented by a guidance scan  $\mathbf{x}_{guid}$  coming from the same magnetic field. Thus, (10) can be solved by embedding an NST engine in the reconstruction pipeline.

The overall structure of our RNST is demonstrated in Figure 1(a). As an optimizer to reconstruct the low-field input image, it contains two main parts in the optimization iteration. The first one is an NST network that provides a set of directional style transferred images from the raw input. As mentioned above, the NST engine works based on the handling of the content image and style image as shown in Figure 1(b). By computing the style and content loss between the input and style guidance image, the NST engine updates the input with respect to this loss combination. After a number of iterations, the output contains content of the original input but has a feature style, or pixel correlations closer to the style image. NST benefits from the fact that it works based on a deep convolutional neural network usually pre-trained on a large-scale dataset such as ImageNet and the network is frozen for feature extraction during the style transfer process [7]. However, the image contents in our work are different from these pre-trained datasets and might lead to a mismatch in feature extraction. Considering this, we applied an online update with the NST engine to search for directions of our gradient descent optimizer. This online update generates multiple candidates from the NST engine with different style transfer levels and these output images with different style transfer levels play the role of guidance for the gradient evaluation. The second part is a line-search gradient descent engine [30] as an iterative approach for reconstruction. Newton’s method provides a faster convergence speed than the classic gradient descent method, yet it requires the calculation of a higher order derivative of the objective function [31]. However, since our reconstruction optimization contains the NST engine outputs and it can be hard to define a numeric derivative of the objective function, we employ a line-search gradient descent as an approximation.

The pseudo-code of our RNST via the line-search gradient descent is formulated as Algorithm 1. Beginning with a noisy lower-field raw input  $x_{in}$  and a higher-field style guidance  $x_{guid}$ , the denoiser  $D$  first generates a denoised image  $x_d$  from the input. Then, a list of style transferred images  $x_t$  are given by the NST engine  $\mathcal{T}$ . Here the subline index  $N_0$  is an initial number and  $N_{step}$  is the step size increase for the iteration number of  $\mathcal{T}$ . After preparation of the style transferred image list  $\mathbf{L}_t$ , a line-search gradient descent is implemented to find the best gradient descent direction with respect to the objective loss  $\mathcal{L}$ . In order to overcome the potential convergence to a local optima of the non-convex objective function, we scan the possible solutions based on the list of style transferred images  $x_t$ , and apply a line-search of different step-sizes  $\tilde{\mu}$  as a further exploration. With a batch of candidates in the list covering multiple step sizes, the best one is selected from the list with respect to the objective function in each iteration. Note that the step-size  $\tilde{\mu}$  can be adjusted dynamically per iteration. For instance, by applying an Armijo step-size rule [32], the value of  $\tilde{\mu}$  can be updated with respect to

the estimation of local gradient and the objective function. Herein, to keep things simple, we set  $\tilde{\mu} = i\mu$ . The gradient direction is calculated by combining the gradient of the style transfer image  $\mathbf{x}_t$  and the denoising image  $\mathbf{x}_d$  to produce an intermediate candidate  $\tilde{\mathbf{x}}$ :

$$\tilde{\mathbf{x}} = \mathbf{x} - \tilde{\mu}(\mathbf{x} - \mathbf{x}_t + \lambda(\mathbf{x} - \mathbf{x}_d)) \quad (11)$$

To evaluate the performance of candidate  $\tilde{\mathbf{x}}$ , a one-step neural style transfer loss is calculated:

$$\begin{aligned} \tilde{\mathbf{x}}' &= \mathcal{T}_{N'_0=1}(\tilde{\mathbf{x}}, \mathbf{x}_{guid}) \\ \mathcal{L}(\tilde{\mathbf{x}}') &= \alpha \mathcal{L}_{content}(\tilde{\mathbf{x}}', \mathbf{x}_{in}) + \beta \mathcal{L}_{style}(\tilde{\mathbf{x}}', \mathbf{x}_{guid}) \end{aligned} \quad (12)$$

And the best candidate is kept as the input for the next iteration.

#### **4. Implementation details**

We applied a VGG-16 network [33] as the base structure of our NST engine. It was pre-trained on general visual recognition tasks [7]. Here, we extracted features from the first 8 layers for style loss calculations and layer 4 for content loss calculations. The network is widely available via the Pytorch package [34]. We further found that implementing L1 loss instead of L2 loss in both the content and style loss can further improve the sharpness of the final images and lead to a better performance. We applied a well-known BM3D [35] as our denoising engine. Recent works have also shown that the Noise-to-Noise (N2N) structure [36] can be a good candidate for the denoising engine especially when clean images are difficult to achieve [37, 38, 39, 40, 41].

For the RNST algorithm, we set  $N_{style} = 3$  and  $N_{line} = 5$ . The NST engine directional steps were set to  $N_0 = 100$  and  $N_{step} = 100$ . The weighting factor ratio in the NST engine was set to  $\alpha//\beta = 10^{-6}$ . Other hyper-parameter details are illustrated in the following section.

## Experiments

### *MRI scanning details*

We tested our RNST method with clinical scans and performed quantitative evaluations. The data was collected on a 3T and 1.5T scanner (Ingenia Philips Healthcare). The measurements were taken using the ELGAN-ECHO MRI protocol [42] for the same subject in both magnetic strengths. It included two concatenated scans with identical geometry and receiver settings implemented, which is called a dual-echo turbo spin-echo (TSE) and a single-echo TSE, combined as a triple TSE (fast spin-echo [FSE]). The scanning is a triple-weighting acquisition including directly acquired (DA) image 1 for proton density-weighted, DA2 for T2-weighted and DA3 for T1-weighted, voxel =  $0.5 \times 0.5 \times 2\text{mm}$ . Echo times = 12 msec, 102 msec for the first and second effective echo; long repetition time = 10 seconds, short repetition time = 5 seconds. Each DA generated 80 slices, leading to 240 slices for each magnetic strength.

We used the unregistered 3T scan as the style guidance and the 1.5T scan as the content images. The resolution for each slice is  $512 \times 512$ . We then performed a 3D registration on the 3T scan corresponding to the 1.5T scan to give the registered 3T scan using 3DSlicer [43, 44]. This registered 3T scan worked as the reconstruction reference in our performance evaluation. We performed two reconstruction tests. The first one used the original 1.5T and 3T scan respectively. For the second one, apart from the original background noise in the 1.5T scans, we further corrupted them with an additive white Gaussian noise (AWGN) level of 0.08 ( $\sigma = 20/255$ ). For the first test, we set  $N_{iter}$  to 10 and  $\mu = 0.13$  and  $\lambda = 0.2$ . For the second test with AWGN, we set  $N_{iter}$  to 50 and  $\mu = 0.15$  and  $\lambda = 0.3$ .

Our RNST reconstruction includes a matched guidance and frozen guidance setup. In the matched guidance setup, the slice number of the guidance image and noisy content image were matched. Note that their image contents were still quite different due to the subject movement. To further demonstrate that RNST benefits from the fact that the guidance  $x_{guid}$  encodes the image style and implicitly represents the reconstruction, we froze the guidance image index to  $i_{guid} = 55$  and performed reconstruction on the truncated brain portion of slices  $i_{brain} = [40,60]$ . During the evaluation, each reconstruction  $\hat{x}$  was compared to the registered 3T scan with the matched slice

index  $x_{registered}$ . Our quantitative metrics include peak signal-to-noise ratio (PSNR) in dB and structural similarity (SSIM):

$$PSNR(\hat{x}, x) = 10 \log_{10} \frac{\max(x)^2}{MSE(\hat{x}, x)} \quad (13)$$

$$SSIM(\hat{x}, x) = \frac{(2\mu_{\hat{x}}\mu_x + c_1)(2\sigma_{\hat{x}x} + c_2)}{(\mu_{\hat{x}}^2 + \mu_x^2 + c_1)(\sigma_{\hat{x}}^2 + \sigma_x^2 + c_2)} \quad (14)$$

Here,  $\hat{x}$  and  $x$  stand for the reconstruction and target image, and  $\mu$  and  $\sigma$  are the average and variance of the image.  $c_1 = (k_1L)^2$ ,  $c_2 = (k_2L)^2$  are two factors to stabilize the division.  $L$  is the dynamic range of the pixel-values. We use a window size of  $7 \times 7$  with  $k_1 = 0.01$  and  $k_2 = 0.03$ .

## Results

We performed RNST with matched guidance over all 80 slices for three DA images. To show the capability of reconstruction with limited style guidance image, we further applied matched guidance and frozen guidance RNST reconstruction tasks for the truncated brain portion regarding  $i_{brain} = [40,60]$  with the frozen guidance index  $i_{guid} = 55$ .

Table 1 and 2 demonstrate our RNST reconstruction metrics. They include one part for evaluation metrics over 80 slices for the matched guidance setup, while the other part demonstrates the metrics focusing on the brain with both matched and frozen guidance setups. Figure 2 illustrates the SSIM performance of matched and frozen setups for all slices. Overall, our RNST framework gave a significant boost in image quality when compared to the registered high-field reference scans. More interestingly, Table 1 and 2 further show that frozen guidance provides a similar level of reconstruction quality compared to matched guidance high-field reconstructions. The performance can be different when another slice was set as the frozen guidance, yet the reconstruction metrics show that our RNST benefits from the fact that the guidance image is used for image style and feature reconstruction reference. The higher-field target is encoded implicitly in the guidance such that the image contents do not need to match with the lower-field noisy scans. Noted that all the RNST reconstructions were performed with the limited scans (240 slices for each magnetic strength) available. Each reconstruction only took one content and one guidance image. The NST engine we embedded is widely available pre-trained on common open-source image datasets instead of on MRI-specific datasets.

Figures 3 and 4 demonstrate example reconstruction slices from matched and frozen guidance reconstruction. Both setups preserved the content details from the low-field scans while the reconstructed images have similar image styles to the registered references. Figures 5 and 6 show reconstructions with red boxes depicting enlarged details and the corresponding error maps. Overall, matched guidance reconstruction provides a slightly cleaner or similar error map compared to the frozen guidance setup in DA1 and 2 for the reconstruction slice. DA3's frozen guidance error map is even slightly cleaner than the matched guidance one. This comes from the fact that the slice we chose in the frozen guidance setup had an overall smaller brain area and lower pixel brightness in the images of DA3 than DA1 and 2 for the reconstruction slice, which led to a stronger punishment for the style

transfer loss during the reconstruction. Overall, both setups significantly reduced the background noise and performed magnetic field transfer reconstruction properly.

In Figures 7 and 8, we demonstrate reconstruction samples for both setups along multiple iterations. Here, we present intermediate steps for iterations 1, 5 and 10, together with their intermediate evaluation metrics and error maps. The figures show that RNST performs reconstruction and noise reduction along iterations with better performance metrics as the iteration number increases. Overall, our experimental results highlight the capability of the RNST framework for limited data MRI reconstruction. This is especially helpful when scanning data is limited, precluding a large-scale deep neural network training and it also has the potential to be applied as an additional refinement to other reconstruction methods.

## Discussion and Conclusion

Typical deep learning-based MRI reconstruction frameworks require task-specific large-scale datasets to function properly. Although they have shown great success, more work needs to be done when it comes to applications where only limited data is available. In this work, we proposed a regularization by neural style transfer (RNST) method for MRI magnetic field transfer reconstruction. RNST utilizes a neural style transfer (NST) engine and a denoiser to reconstruct higher-field quality images from a noisy lower-field input. Thanks to its NST engine, RNST can perform reconstruction with limited data and no specific need to train on a large-scale task-specific dataset.

We tested RNST using clinical 1.5T and 3T MRI scans and provided quantitative evaluations. Our results showed that RNST can provide competitive image reconstruction qualities with limited data even without matched guidance. Although our experiment focused on MRI, it can be brought to other applications. Alternatively, it can also serve as an additional refinement process for other reconstruction tasks.

We would like to highlight some limitations and future directions for the current work. As RNST performs reconstruction in an iterative way, it consumes more time for image processing. Plus, RNST can lead to unstable performance if the images deviate too much from the feature extraction network's pre-trained contents and requires good tunings of the hyper-parameters. Thus, one future direction would be to improve the efficiency of the optimizer and to combine more advanced generative deep learning methods such as generative adversarial networks (GANs) and denoising diffusion probabilistic models (DDPMs), which can be done by incorporating a few-shot learning strategy with a pre-training on a broader image content dataset.

## Figures, tables and algorithms

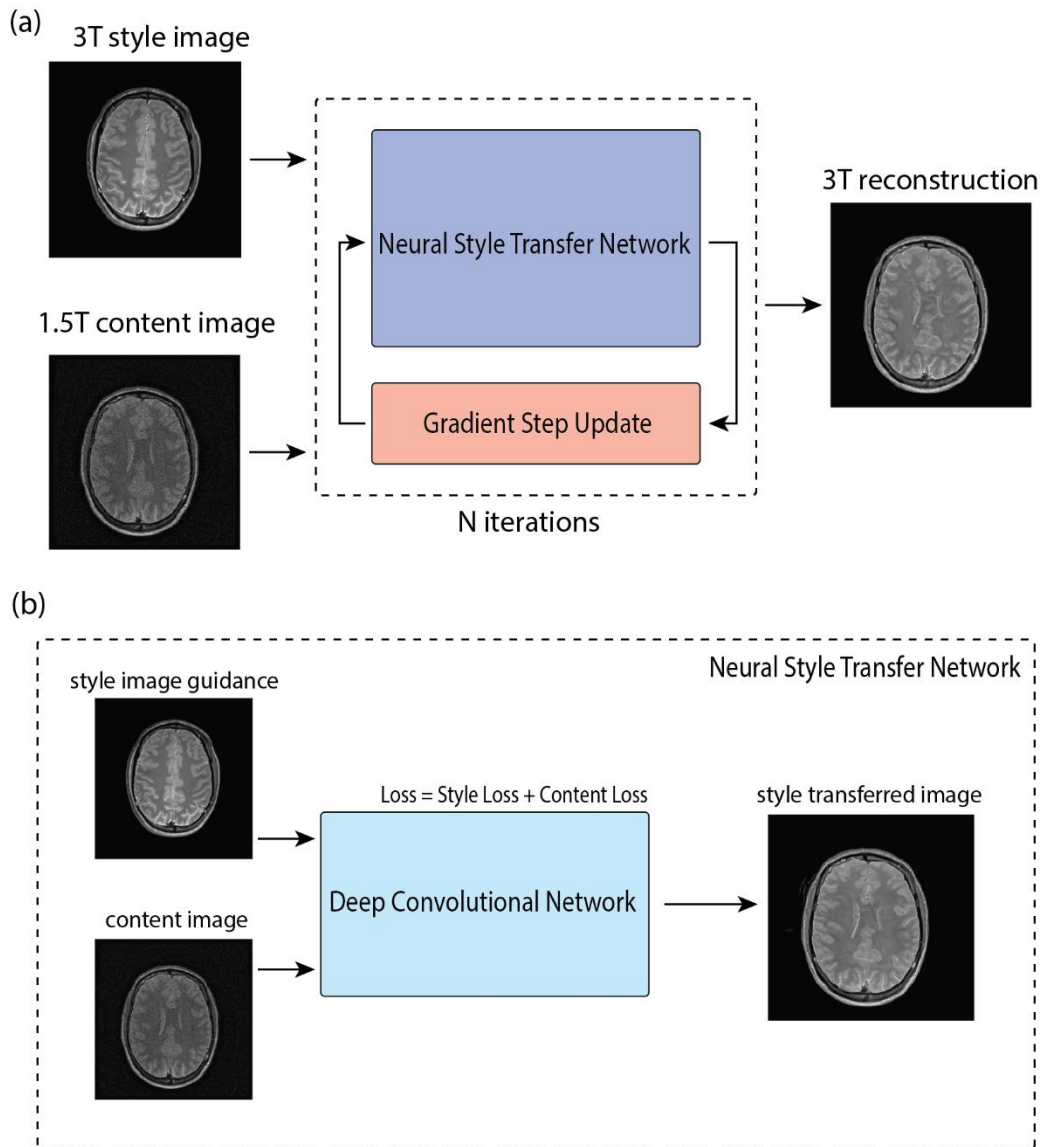


**Figure 1.** Framework of our regularization by neural style transfer (RNST) algorithm. (a) shows the overall structure of RNST. It contains two main parts in the optimization iteration. The first one is a neural style transfer (NST) network that provides a set of style transferred images from the input. Then, a gradient step update is applied for denoising and reconstruction. The final reconstruction is generated after N iterations. (b) demonstrates a closer look at the NST network. It takes a style image as guidance and a content image for reconstruction. The loss is a combination of the style loss measuring the feature correlations among multiple layers and a content loss measuring the content difference between the output and content feature maps.

---

**Algorithm 1:** RNST via Line-search Gradient Descent

---

```
1: Input: Given  $\lambda, \mu, \alpha, \beta, \mathbf{x}_{in}, \mathbf{x}_{guid}$ 
2: Initialization:  $\mathcal{D}, \mathcal{T}$ 
3:  $\mathbf{x} \leftarrow \mathbf{x}_{in}$ 
4: for  $k = 1, 2, \dots, N_{iter}$  do:
5:      $\mathbf{x}_d = \mathcal{D}(\mathbf{x})$ 
6:      $\mathcal{L}^* = \mathcal{L}_0$ 
7:      $L_t = \{\}$ 
8:     for  $j = 1, 2, \dots, N_{style}$  do:
9:          $\mathbf{x}_t = \mathcal{T}_{N_0+jN_{step}}(\mathbf{x}_d, \mathbf{x}_{guid})$ 
10:         $L_t$  add  $\mathbf{x}_t$ 
11:    end for
12:    Line-search Gradient Descent:
13:    for  $i = 1, 2, \dots, N_{line}$  do:
14:         $\tilde{\mu} = i \cdot \mu$ 
15:        for  $x_t$  in  $L_t$  do:
16:             $\tilde{\mathbf{x}} = \mathbf{x} - \tilde{\mu}(\mathbf{x} - \mathbf{x}_t + \lambda(\mathbf{x} - \mathbf{x}_d))$ 
17:             $\tilde{\mathbf{x}}' = \mathcal{T}_{N'_0=1}(\tilde{\mathbf{x}}, \mathbf{x}_{guid})$ 
18:             $\mathcal{L}(\tilde{\mathbf{x}}') = \alpha \mathcal{L}_{content}(\tilde{\mathbf{x}}', \mathbf{x}_{in}) + \beta \mathcal{L}_{style}(\tilde{\mathbf{x}}', \mathbf{x}_{guid})$ 
19:            if  $\mathcal{L}(\tilde{\mathbf{x}}') < \mathcal{L}^*$  then
20:                 $\mathbf{x}_{out} = \tilde{\mathbf{x}}$ 
21:                 $\mathcal{L}^* = \mathcal{L}(\tilde{\mathbf{x}}')$ 
22:            end if
23:        end for
24:    end for
25:     $\mathbf{x} = \mathbf{x}_{out}$ 
26: end for
27: Result: The output is  $\mathbf{x}$ 
```

---

**Algorithm 1.** Pseudo-code of our RNST via line-search gradient descent algorithm.

|                                 | PSNR  |       |       | SSIM   |        |        |
|---------------------------------|-------|-------|-------|--------|--------|--------|
|                                 | DA1   | DA2   | DA3   | DA1    | DA2    | DA3    |
| All slices                      |       |       |       |        |        |        |
| Input                           | 20.48 | 20.34 | 20.81 | 0.2659 | 0.2327 | 0.2427 |
| Reconstruction                  | 21.04 | 23.61 | 22.99 | 0.7605 | 0.7716 | 0.7748 |
| Brain portion                   |       |       |       |        |        |        |
| Input                           | 21.24 | 21.10 | 22.50 | 0.3464 | 0.3071 | 0.3215 |
| Matched guidance reconstruction | 22.83 | 25.01 | 25.07 | 0.8178 | 0.8181 | 0.8210 |
| Frozen guidance reconstruction  | 22.68 | 24.60 | 24.96 | 0.7917 | 0.8041 | 0.8114 |

**Table 1.** Evaluation metrics of RNST reconstructions on the original scan.

|                                 | PSNR  |       |       | SSIM   |        |        |
|---------------------------------|-------|-------|-------|--------|--------|--------|
|                                 | DA1   | DA2   | DA3   | DA1    | DA2    | DA3    |
| All slices                      |       |       |       |        |        |        |
| Input                           | 18.39 | 18.29 | 18.53 | 0.1055 | 0.1026 | 0.0882 |
| Reconstruction                  | 20.75 | 22.81 | 22.37 | 0.7608 | 0.7664 | 0.7698 |
| Brain portion                   |       |       |       |        |        |        |
| Input                           | 18.89 | 18.77 | 19.55 | 0.1288 | 0.1293 | 0.1005 |
| Matched guidance reconstruction | 22.64 | 24.16 | 24.91 | 0.8183 | 0.8181 | 0.8212 |
| Frozen guidance reconstruction  | 22.73 | 23.81 | 25.38 | 0.8116 | 0.8114 | 0.8313 |

**Table 2.** Evaluation metrics of RNST reconstructions with additional noise.

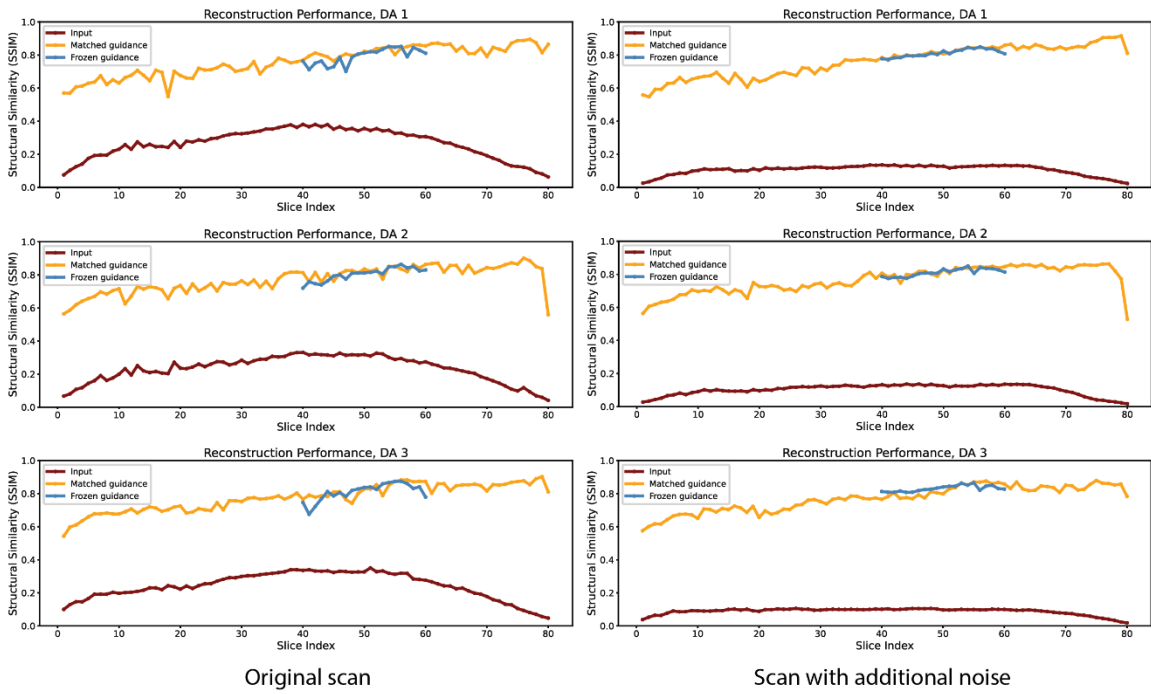


**Figure 2.** Quantitative reconstruction evaluation of RNST for matched and frozen guidance setups among three DAs.

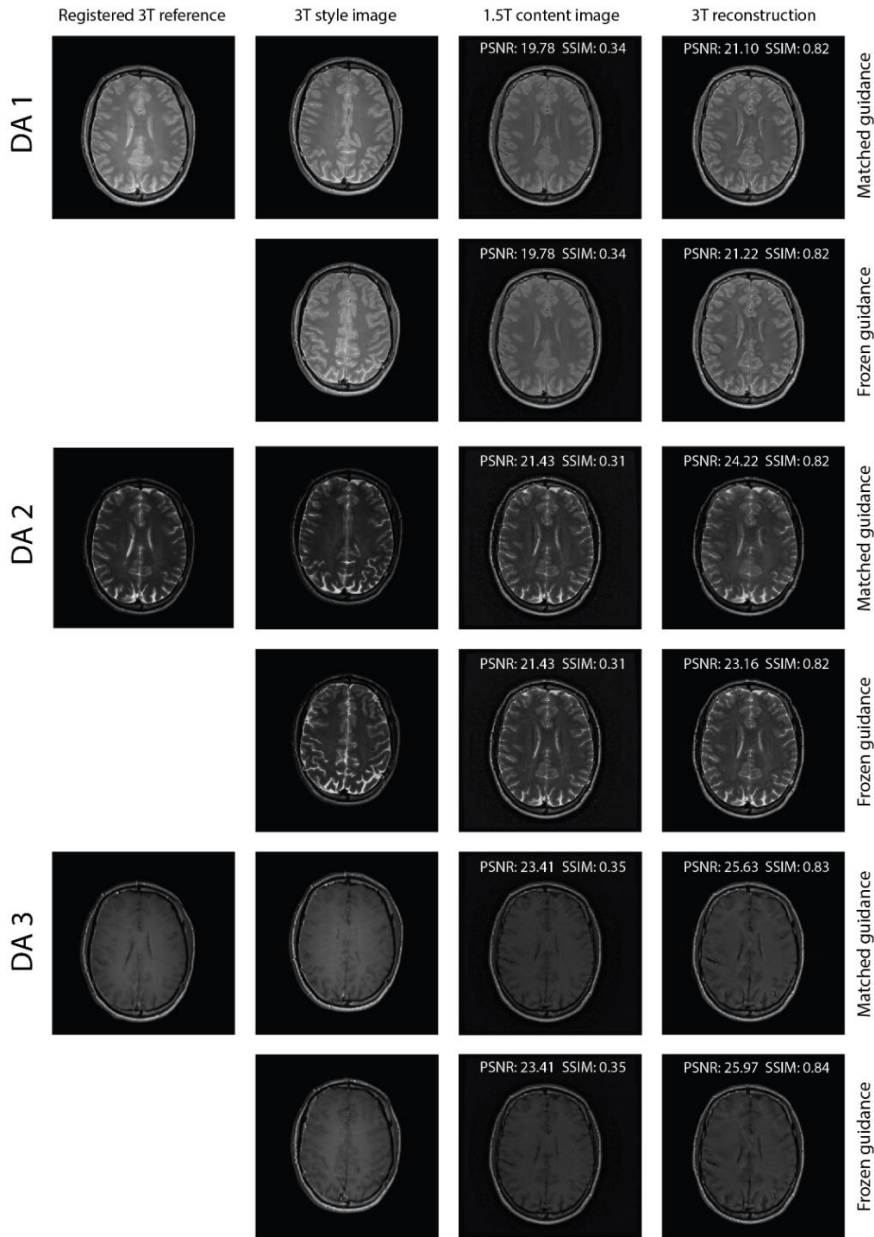


**Figure 3.** Reconstruction results of our RNST over the original scans. The algorithm took a 3T style image as guidance and a 1.5T content image as input to yield a 3T style reconstruction. The scans include three directly acquired (DA) images: DA1 to 3. For each DA, the evaluation metrics are measured between the registered 3T reference and the 1.5T input content image or the final 3T reconstruction. We demonstrate two setups: matched guidance and frozen guidance. In matched guidance setup, the style image had the same slice number so that they have similar image content. In frozen guidance setup, we froze the style image to be the same among reconstruction for slices. This figure shows that RNST can significantly boost image qualities without the need to train on a large-scale MRI dataset, which is especially beneficial when data is limited.

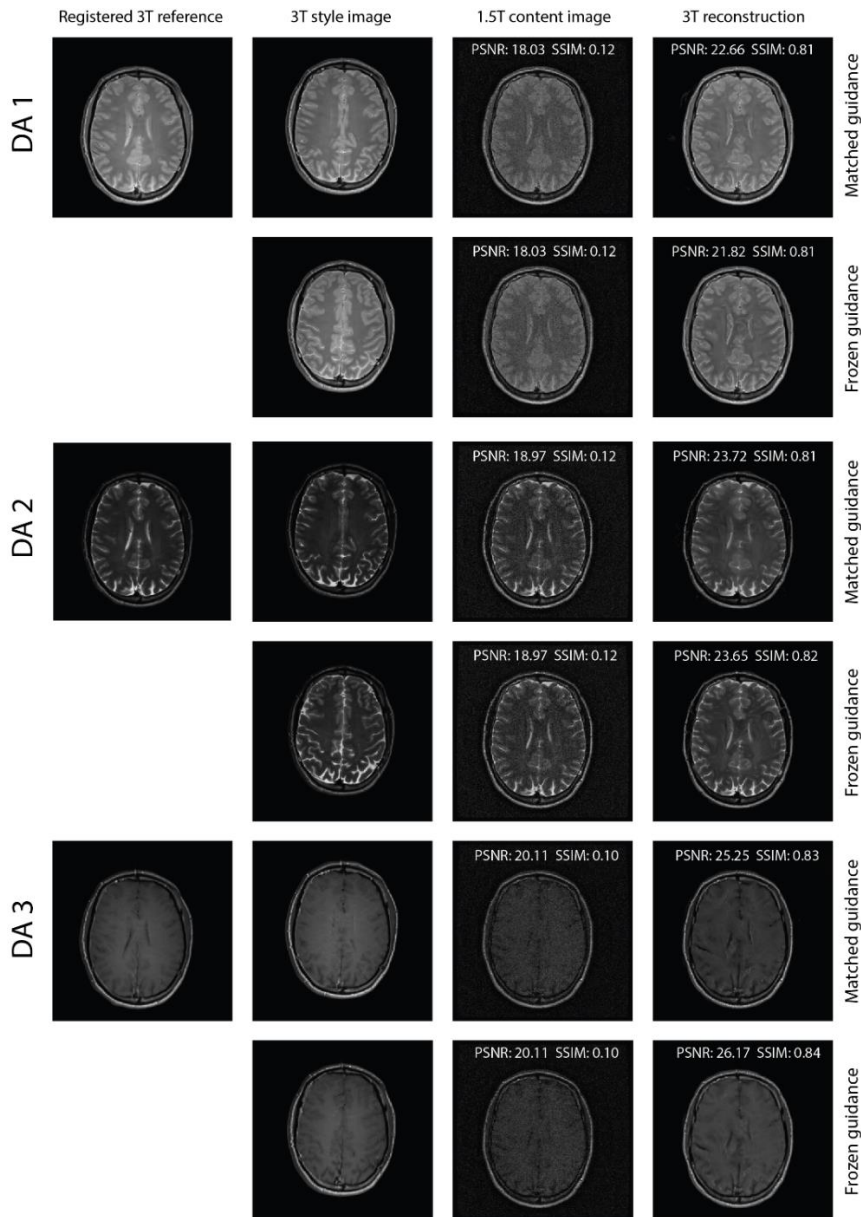


**Figure 4.** Reconstruction results of our RNST with additional noise. The algorithm took a 3T style image as guidance and a 1.5T content image as input to yield a 3T style reconstruction. The scans include three directly acquired (DA) images: DA1 to 3. For each DA, the evaluation metrics are measured between the registered 3T reference and the 1.5T input content image or the final 3T reconstruction. We demonstrate two setups: matched guidance and frozen guidance. In matched guidance setup, the style image had the same slice number so that they have similar image content. In frozen guidance setup, we froze the style image to be the same among reconstruction for slices. This figure shows that RNST can significantly boost image qualities without the need to train on a large-scale MRI dataset, which is especially beneficial when data is limited.

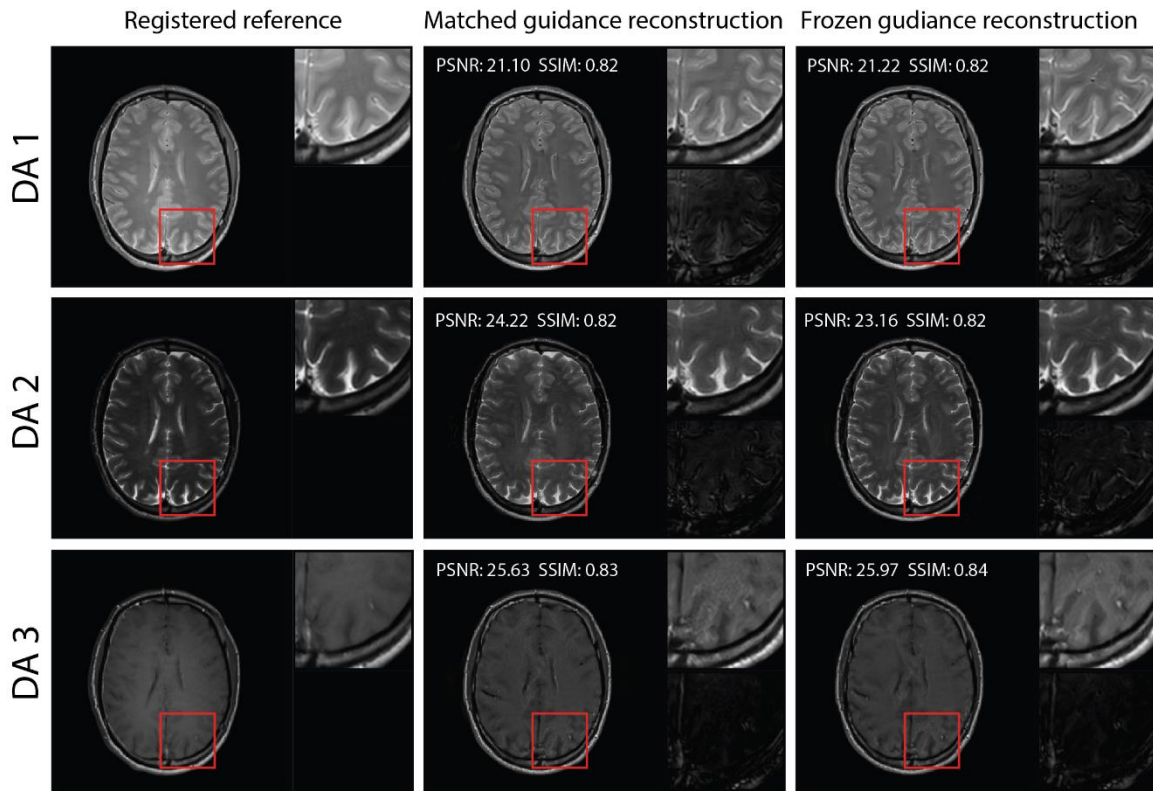


**Figure 5.** Visual illustration of RNST results for matched and frozen guidance setups for three DAs on the original scans. The image details highlighted in the red box in each figure were enlarged on the upper right side, with the corresponding error maps compared to the registered reference showing on the lower right side. This figure shows that both matched and frozen guidance setup provide similar levels of reconstruction performance.

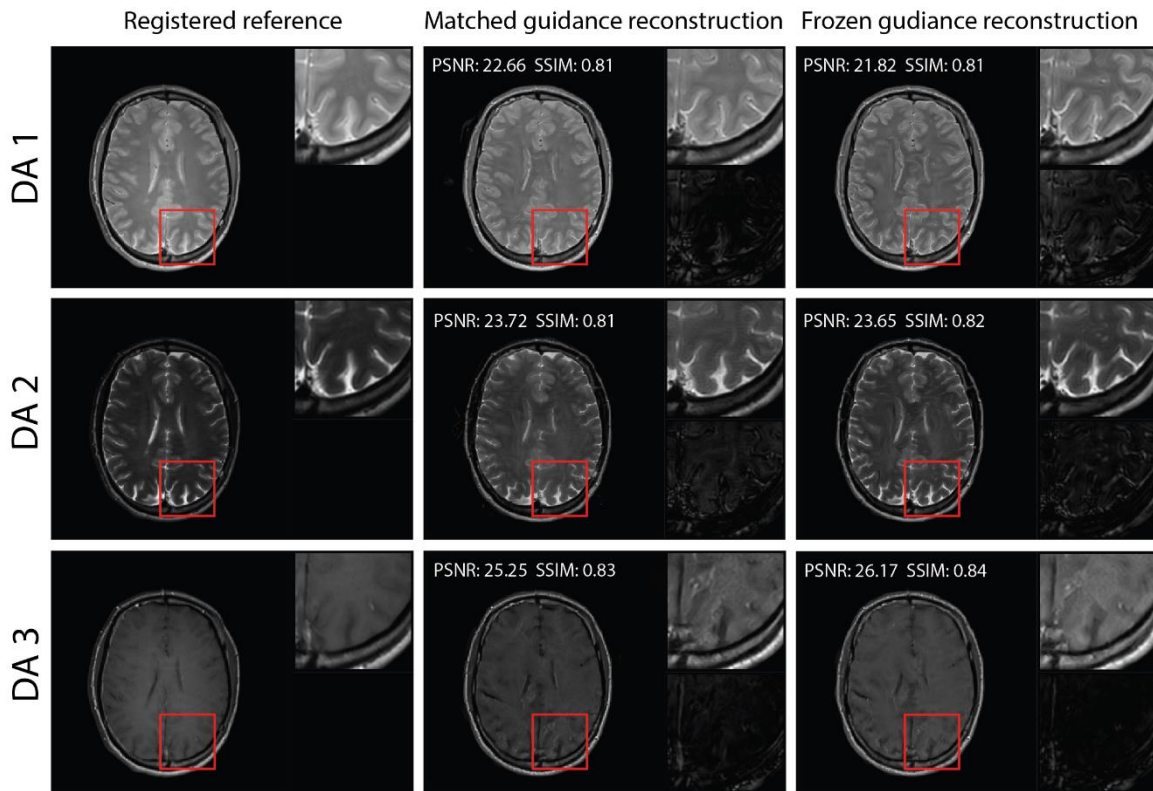


**Figure 6.** Visual illustration of RNST results for matched and frozen guidance setups for three DAs with additional noise. The image details highlighted in the red box in each figure were enlarged on the upper right side, with the corresponding error maps compared to the registered reference showing on the lower right side. This figure shows that both matched and frozen guidance setup provide similar levels of reconstruction performance.

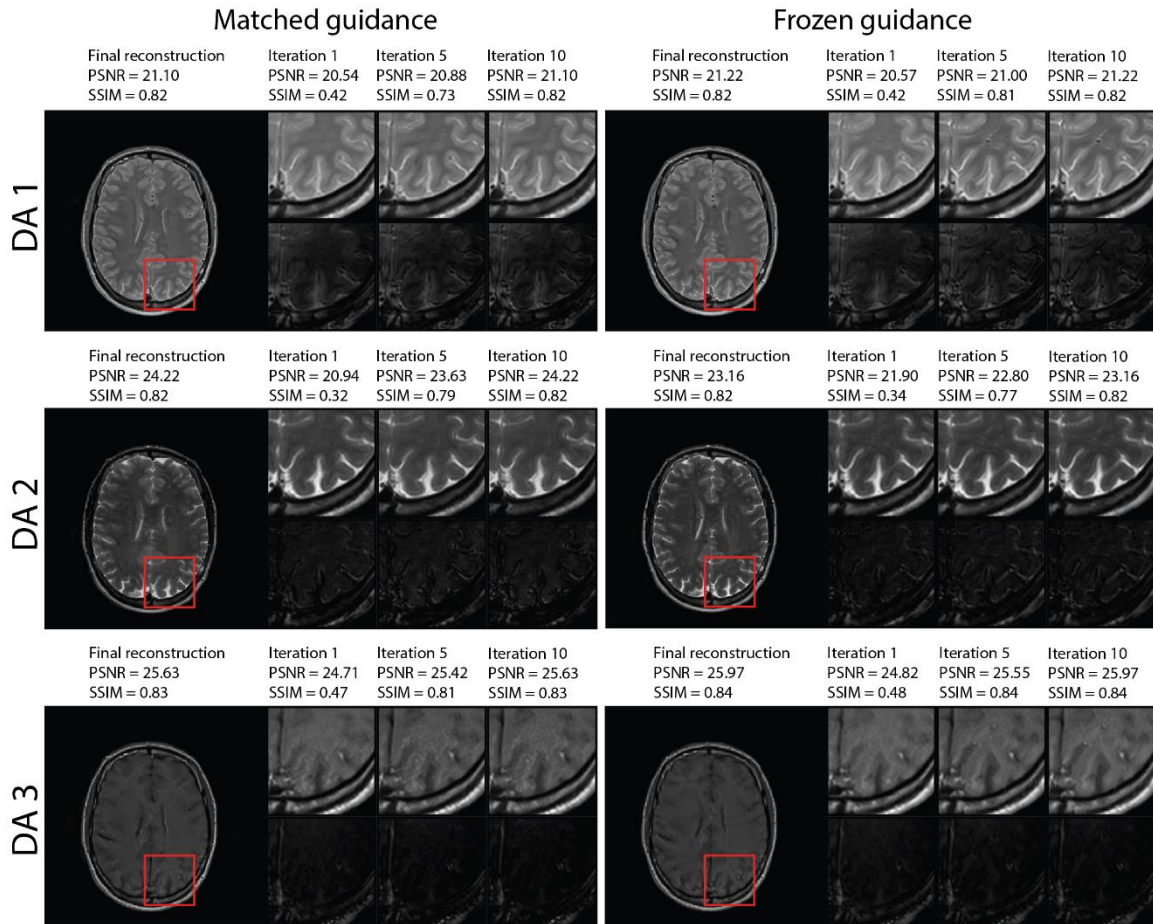


**Figure 7.** Visual illustration and quantitative metrics of the RNST reconstructions along iterations on the original scans. The image details highlighted in the red box in each figure were enlarged on the upper right side, with the corresponding error maps compared to the registered reference showing on the lower right side. PSNR and SSIM are labeled with the iteration numbers. The figure shows the evolution of RNST performing reconstruction and noise reduction along iterations.

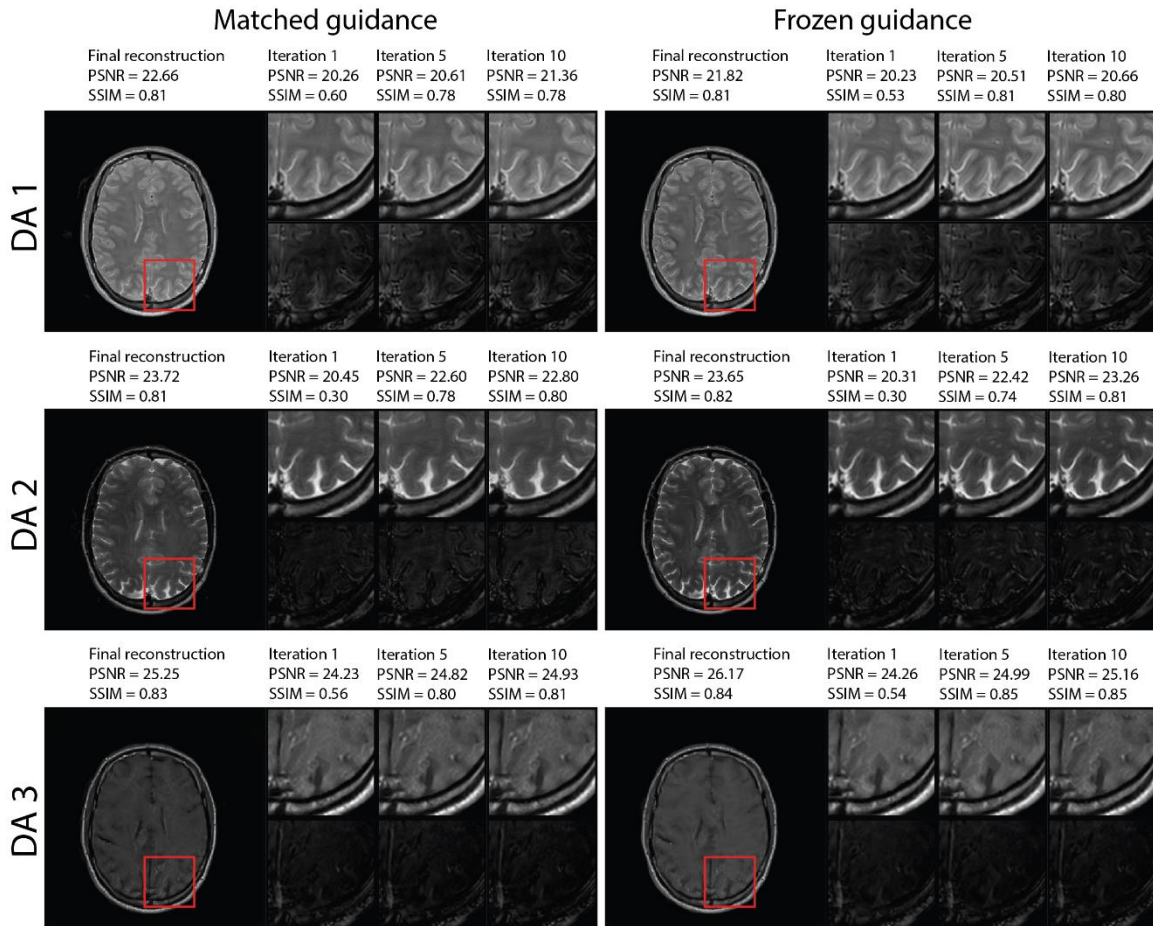


**Figure 8.** Visual illustration and quantitative metrics of the RNST reconstructions along iterations with additional noise. The image details highlighted in the red box in each figure were enlarged on the upper right side, with the corresponding error maps compared to the registered reference showing on the lower right side. PSNR and SSIM are labeled with the iteration numbers. The figure shows the evolution of RNST performing reconstruction and noise reduction along iterations.

## References

- [1] Zbontar, J., Knoll, F., Sriram, A., Muckley, M. J., Bruno, M., Defazio, A., et al. fastMRI: An Open Dataset and Benchmarks for Accelerated MRI. CoRR, abs/1811.08839. (2018). <http://arxiv.org/abs/1811.08839>
- [2] Sriram, A., Zbontar, J., Murrell, T., Zitnick, C. L., Defazio, A., & Sodickson, D. K. GrappaNet: Combining Parallel Imaging with Deep Learning for Multi-Coil MRI Reconstruction. (2020). <https://arxiv.org/abs/1910.12325>
- [3] Eo, T., Jun, Y., Kim, T., Jang, J., Lee, H.-J., & Hwang, D. KIKI-net: cross-domain convolutional neural networks for reconstructing undersampled magnetic resonance images. Magnetic Resonance in Medicine, 80(5), 2188–2201. (2018). <https://doi.org/https://doi.org/10.1002/mrm.27201>
- [4] Souza, R., & Frayne, R. A Hybrid Frequency-Domain/Image-Domain Deep Network for Magnetic Resonance Image Reconstruction. 2019 32nd SIBGRAPI Conference on Graphics, Patterns and Images (SIBGRAPI), 257–264. (2019). <https://doi.org/10.1109/SIBGRAPI.2019.00042>
- [5] Hammernik, K., Klatzer, T., Kobler, E., Recht, M. P., Sodickson, D. K., Pock, T., & Knoll, F. Learning a variational network for reconstruction of accelerated MRI data. Magnetic Resonance in Medicine, 79(6), 3055–3071. (2018). <https://doi.org/https://doi.org/10.1002/mrm.26977>
- [6] Sriram, A., Zbontar, J., Murrell, T., Defazio, A., Zitnick, C. L., Yakubova, N., Knoll, F., & Johnson, P. End-to-End Variational Networks for Accelerated MRI Reconstruction. (2020). <https://arxiv.org/abs/2004.06688>
- [7] Gatys, L. A., Ecker, A. S., & Bethge, M. A Neural Algorithm of Artistic Style. (2015). <https://arxiv.org/abs/1508.06576>
- [8] Goodfellow, I. J., Pouget-Abadie, J., Mirza, M., Xu, B., Warde-Farley, D., Ozair, S., Courville, A., & Bengio, Y. Generative Adversarial Networks. (2014). <https://arxiv.org/abs/1406.2661>
- [9] Chen, D., Yuan, L., Liao, J., Yu, N., & Hua, G. Stereoscopic Neural Style Transfer. Proceedings of the IEEE Conference on Computer Vision and Pattern Recognition (CVPR). (2018, June).
- [10] Gatys, L. A., Bethge, M., Hertzmann, A., & Shechtman, E. Preserving Color in Neural Artistic Style Transfer. CoRR, abs/1606.05897. (2016). <http://arxiv.org/abs/1606.05897>

- [11] Luan, F., Paris, S., Shechtman, E., & Bala, K. Deep Photo Style Transfer. Proceedings of the IEEE Conference on Computer Vision and Pattern Recognition (CVPR). (2017, July).
- [12] Jing, Y., Yang, Y., Feng, Z., Ye, J., Yu, Y., & Song, M. Neural Style Transfer: A Review. IEEE Transactions on Visualization and Computer Graphics, 26(11), 3365–3385. (2020).  
<https://doi.org/10.1109/TVCG.2019.2921336>
- [13] Azadi, S., Fisher, M., Kim, V. G., Wang, Z., Shechtman, E., & Darrell, T. Multi-Content GAN for Few-Shot Font Style Transfer. Proceedings of the IEEE Conference on Computer Vision and Pattern Recognition (CVPR). (2018, June).
- [14] Zhang, L., Ji, Y., Lin, X., & Liu, C. Style Transfer for Anime Sketches with Enhanced Residual U-net and Auxiliary Classifier GAN. 2017 4th IAPR Asian Conference on Pattern Recognition (ACPR), 506–511. (2017). <https://doi.org/10.1109/ACPR.2017.61>
- [15] Shaban, M. T., Baur, C., Navab, N., & Albarqouni, S. Staingan: Stain Style Transfer for Digital Histological Images. 2019 IEEE 16th International Symposium on Biomedical Imaging (ISBI 2019), 953–956. (2019). <https://doi.org/10.1109/ISBI.2019.8759152>
- [16] Lin, C.-T., Huang, S.-W., Wu, Y.-Y., & Lai, S.-H. GAN-Based Day-to-Night Image Style Transfer for Nighttime Vehicle Detection. IEEE Transactions on Intelligent Transportation Systems, 22(2), 951–963. (2021). <https://doi.org/10.1109/TITS.2019.2961679>
- [17] Ho, J., Jain, A., & Abbeel, P. Denoising Diffusion Probabilistic Models. (2020).  
<https://arxiv.org/abs/2006.11239>
- [18] Saharia, C., Ho, J., Chan, W., Salimans, T., Fleet, D. J., & Norouzi, M. Image Super-Resolution via Iterative Refinement. IEEE Transactions on Pattern Analysis and Machine Intelligence, 45(4), 4713–4726. (2023). <https://doi.org/10.1109/TPAMI.2022.3204461>
- [19] Romano, Y., Elad, M., & Milanfar, P. The Little Engine that Could: Regularization by Denoising (RED). CoRR, abs/1611.02862. (2016). <http://arxiv.org/abs/1611.02862>
- [20] Venkatakrisnan, S. V., Bouman, C. A., & Wohlberg, B. Plug-and-Play priors for model based reconstruction. 2013 IEEE Global Conference on Signal and Information Processing, 945–948. (2013).  
<https://doi.org/10.1109/GlobalSIP.2013.6737048>
- [21] Mataev, G., Milanfar, P., & Elad, M. DeepRED: Deep Image Prior Powered by RED. Proceedings of the IEEE/CVF International Conference on Computer Vision (ICCV) Workshops. (2019, October).

- [22] Metzler, C., Schniter, P., Veeraraghavan, A., & Baraniuk, R. prDeep: Robust Phase Retrieval with a Flexible Deep Network. In J. Dy & A. Krause (Eds.), Proceedings of the 35th International Conference on Machine Learning (Vol. 80, pp. 3501–3510). (2018).
- [23] Wu, Z., Sun, Y., Liu, J., & Kamilov, U. Online Regularization by Denoising with Applications to Phase Retrieval. Proceedings of the IEEE/CVF International Conference on Computer Vision (ICCV) Workshops. (2019, October).
- [24] Gan, W., Eldeniz, C., Liu, J., Chen, S., An, H., & Kamilov, U. S. Image Reconstruction for MRI using Deep CNN Priors Trained without Groundtruth. 2020 54th Asilomar Conference on Signals, Systems, and Computers, 475–479. (2020). <https://doi.org/10.1109/IEEECONF51394.2020.9443403>
- [25] Gan, W., Sun, Y., Eldeniz, C., Liu, J., An, H., & Kamilov, U. S. Deformation-Compensated Learning for Image Reconstruction without Ground Truth. (2021). <https://arxiv.org/abs/2107.05533>
- [26] Liu, J., Sun, Y., Eldeniz, C., Gan, W., An, H., & Kamilov, U. S. RARE: Image Reconstruction Using Deep Priors Learned Without Groundtruth. IEEE Journal of Selected Topics in Signal Processing, 14(6), 1088–1099. (2020). <https://doi.org/10.1109/jstsp.2020.2998402>
- [27] Zhang, Q., & Zhu, S. Visual interpretability for deep learning: a survey. Frontiers of Information Technology & Electronic Engineering, 19(1), 27–39. (2018). <https://doi.org/10.1631/FITEE.1700808>
- [28] Mahendran, A., & Vedaldi, A. Understanding Deep Image Representations by Inverting Them. Proceedings of the IEEE Conference on Computer Vision and Pattern Recognition (CVPR). (2015, June).
- [29] Gatys, L. A., Ecker, A. S., & Bethge, M. Texture synthesis and the controlled generation of natural stimuli using convolutional neural networks. CoRR, abs/1505.07376. (2015). <http://arxiv.org/abs/1505.07376>
- [30] Stanimirović, P.S., Miladinović, M.B. Accelerated gradient descent methods with line search. Numer Algor 54, 503–520 (2010). <https://doi.org/10.1007/s11075-009-9350-8>
- [31] Deuffhard, P. Newton methods for nonlinear problems: affine invariance and adaptive algorithms, volume 35. Springer Science & Business Media, 2005.
- [32] Larry Armijo, L. Minimization of functions having lipschitz continuous first partial derivatives. Pacific Journal of mathematics, 16(1):1–3, 1966.

- [33] Simonyan, K., & Zisserman, A. Very Deep Convolutional Networks for Large-Scale Image Recognition. (2015). <https://arxiv.org/abs/1409.1556>
- [34] Paszke, A., Gross, S., Massa, F., Lerer, A., Bradbury, J., Chanan, G., et al. PyTorch: An Imperative Style, High-Performance Deep Learning Library. (2019). <https://arxiv.org/abs/1912.01703>
- [35] Dabov, K., Foi, A., Katkovnik, V., & Egiazarian, K. Image Denoising by Sparse 3-D Transform-Domain Collaborative Filtering. *IEEE Transactions on Image Processing*, 16(8), 2080–2095. (2007). <https://doi.org/10.1109/TIP.2007.901238>
- [36] Lehtinen, J., Munkberg, J., Hasselgren, J., Laine, S., Karras, T., Aittala, M., & Aila, T. Noise2Noise: Learning Image Restoration without Clean Data. (2018). <https://arxiv.org/abs/1803.04189>
- [37] Quan, Y., Chen, M., Pang, T., & Ji, H. Self2Self With Dropout: Learning Self-Supervised Denoising From Single Image. *Proceedings of the IEEE/CVF Conference on Computer Vision and Pattern Recognition (CVPR)*. (2020, June).
- [38] Krull, A., Buchholz, T.-O., & Jug, F. Noise2Void - Learning Denoising From Single Noisy Images. *Proceedings of the IEEE/CVF Conference on Computer Vision and Pattern Recognition (CVPR)*. (2019, June).
- [39] Guo, S., Yan, Z., Zhang, K., Zuo, W., & Zhang, L. Toward Convolutional Blind Denoising of Real Photographs. *Proceedings of the IEEE/CVF Conference on Computer Vision and Pattern Recognition (CVPR)*. (2019, June).
- [40] Huang, T., Li, S., Jia, X., Lu, H., & Liu, J. Neighbor2Neighbor: Self-Supervised Denoising From Single Noisy Images. *Proceedings of the IEEE/CVF Conference on Computer Vision and Pattern Recognition (CVPR)*, 14781–14790. (2021).
- [41] Pang, T., Zheng, H., Quan, Y., & Ji, H. Recorrupted-to-Recorrupted: Unsupervised Deep Learning for Image Denoising. *Proceedings of the IEEE/CVF Conference on Computer Vision and Pattern Recognition (CVPR)*, 2043–2052. (2021).
- [42] McNaughton, R., Pieper, C., Sakai, O., Rollins, J. V., Zhang, X., Kennedy, D. N., Frazier, J. A., Douglass, L., Heeren, T., Fry, R. C., O'Shea, T. M., Kuban, K. K., Jara, H., & ELGAN-ECHO Study Investigators Quantitative MRI Characterization of the Extremely Preterm Brain at Adolescence: Atypical versus Neurotypical Developmental Pathways. *Radiology*, 304(2), 419–428. (2022). <https://doi.org/10.1148/radiol.210385>

[43] Pieper, S., Halle, M., & Kikinis, R. 3D Slicer. 2004 2nd IEEE International Symposium on Biomedical Imaging: Nano to Macro (IEEE Cat No. 04EX821), 632-635 Vol. 1. (2004).

<https://doi.org/10.1109/ISBI.2004.1398617>

[44] Fedorov, A., Beichel, R., Kalpathy-Cramer, J., Finet, J., Fillion-Robin, J. C., Pujol, S., Bauer, C., Jennings, D., Fennessy, F., Sonka, M., Buatti, J., Aylward, S., Miller, J. V., Pieper, S., & Kikinis, R. 3D Slicer as an image computing platform for the Quantitative Imaging Network. *Magnetic resonance imaging*, 30(9), 1323–1341. (2012). <https://doi.org/10.1016/j.mri.2012.05.001>